This article has been accepted for publication in a future issue of this journal, but has not been fully edited. Content may change prior to final publication. Citation information: DOI 10.1109/JSTQE.2014.2381464, IEEE Journal of Selected Topics in Quantum Electronics

Range Extension of a Bimorph Varifocal Micromirror through Actuation by a Peltier Element

Alan Paterson, Ralf Bauer, Li Li, Walter Lubeigt, Deepak Uttamchandani, Senior Member, IEEE

Abstract—A bimorph varifocal micromirror actuated thermoelectrically by a Peltier element is reported. The single crystal silicon micromirror is 1.2 mm in diameter with a centered 1 mm diameter gold coating for broadband reflection. The actuation principle is capable of varying the micromirror temperature above and below the ambient temperature, which contributed to a 57% improvement in the addressable curvature range in comparison to previously reported electrothermal and optothermal actuation techniques for the device. Altering the device temperature from 10 °C to 100 °C provided a mirror surface radius of curvature variation from 19.2 mm to 30.9 mm respectively. The experimental characterization of the micromirror was used as a basis for accurate finite element modeling of the device and its actuation. Negligible optical aberrations are observed over the operating range, enabling effectively aberration-free imaging. Demonstration in an optical imaging system illustrated sharp imaging of objects over a focal plane variation of 212 mm.

Index Terms—Varifocal micromirror (VFM), Silicon-on-insulator multi-user MEMS processes (SOIMUMPs), Imaging, Thermal actuation, Finite element analysis, Optical MEMS.

I. Introduction

MEMS with varifocal properties have been demonstrated to be beneficial in biomedical imaging applications, particularly where spatial limitations are incurred. Varifocal micromirrors (VFMs) provide the necessary requirements to produce compact, high quality imaging systems. This was highlighted by Dickensheets [1] with focus on confocal microscopy and optical coherence tomography (OCT). In confocal microscopy the use of a VFM [2], [3] or a tunable microlens for focal adjustments has been reported [4]. A confocal laser scanning endoscope was demonstrated using a VFM with scanning capability [5]. OCT [6] and multiphoton scanning microscopy [7] have also been achieved using VFMs.

Typically VFM actuation mechanisms can be separated into four main categories: electrostatic [8]-[13], piezoelectric [14]-[16], pneumatic [17] and electrothermal [18], [19]. Optothermal actuation via a laser was also reported [19]. A combination of electrostatic and pneumatic actuation was recently demonstrated to achieve convex and concave VFM surfaces [20]. An electrostatically-actuated VFM with simultaneous scanning capability has been reported by Sasaki et al [21], achieving a focal plane tuning range from -128 mm to +98 mm. The focal power of their micromirror was demonstrated to fluctuate by less than 1% while simultaneous scanning was performed. Lukes and Dickensheets [12] reported a SU-8 deformable membrane mirror which was capable of 137 µm of focal tuning range through electrostatic actuation in an optical microscope with 42x magnification.

In our previous work [19], a 1.2 mm diameter single crystal silicon micromirror with a 1 mm diameter gold coating, forming a bimorph VFM, was characterized using two actuation techniques. These were electrothermal actuation, by applying a current through the serpentine suspension beams connecting the device to the silicon substrate, and optothermal actuation, by applying laser heating to the rear side of the mirror. Implementation of the VFM in an imaging system demonstrated a focal plane variation of 134 mm, over which sharp imaging could be observed. However, limitations were observed using these techniques. The electrothermal technique was limited by the heat capacity of the serpentine suspension beams as current-flow increased, whilst the stability of both the electrothermal and optothermal actuation was sensitive to ambient temperature. Furthermore, these types of actuation could only achieve a temperature increase from the ambient temperature level.

In this paper we report a new actuation technique for VFMs using a thermoelectric (Peltier) element, which improves the focal plane variation of the imaging system by over 50% compared to [19] and does not exhibit the mentioned limitations. This actuation technique is independent of ambient temperature fluctuations and can provide stable temperatures above and below the ambient temperature level. A finite element analysis (FEA) of the device behavior is described in section II, where consideration of thin-film material properties allowed an overlap of simulated results and experimental characteristics. Analysis of the thermoelectric actuation through evaluation of the Zernike coefficients for varying mirror actuation is described in section III, while the

Manuscript submitted October 3, 2014; revised December 7, 2014.

Alan Paterson, Ralf Bauer, Walter Lubeigt and Deepak Uttamchandani are with the Centre for Microsystems and Photonics, Department of Electronic and Electrical Engineering, University of Strathclyde, Glasgow, G1 1XW, UK (e-mail: alan.paterson.2013@uni.strath.ac.uk, ralf.bauer@strath.ac.uk, walter.lubeigt@strath.ac.uk, d.uttamchandani@strath.ac.uk).

Li Li was with the Centre for Microsystems and Photonics, Department of Electronic and Electrical Engineering, University of Strathclyde and is now with the CNOOC, Beijing, China (email: lili55@cnooc.com.cn).

This article has been accepted for publication in a future issue of this journal, but has not been fully edited. Content may change prior to final publication. Citation information: DOI 10.1109/JSTQE.2014.2381464, IEEE Journal of Selected Topics in Quantum Electronics

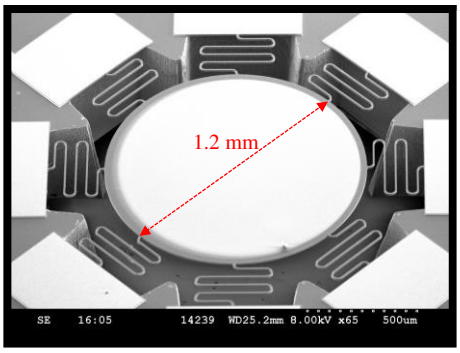

Fig. 1: SEM image of the VFM, showing the 1.2 mm diameter single crystal silicon micromirror and the 1 mm diameter concentric layer of gold deposited on the micromirror surface.

mirror implementation in an optical imaging system is described in section IV. These illustrate that the VFM manifests near-aberration-free imaging using this actuation principle. Demonstration of this Peltier based actuation technique for VFMs also shows the potential for using thin-film thermoelectric coatings, such as Sb_2Te_3 [22] or Bi_2Te_3 [23]. This technology has been reported for power generation [24], cooling and temperature sensing [25] but has not yet been investigated for MEMS-scale imaging applications. An actuation technique of this nature would allow direct control of the device temperature with a considerable reduction in the size of the system.

II. Device Characterization

A. Fabrication and Design

The VFM was fabricated using the silicon-on-insulator multi-user MEMS process (SOIMUMPs) from MEMSCAP Inc., details of which can be found in [26]. The VFM comprises a 10 µm thick device layer of phosphorus-doped single crystal silicon and a 0.65 µm thick layer of gold. The silicon micromirror has a diameter of 1.2 mm, with the 1 mm diameter gold coating deposited concentrically on its surface using electron-beam deposition. This produces a bimorph micromirror with a broadband reflection coating. Eight radially distributed serpentine suspension beams connect the VFM to the 400 µm thick silicon substrate. The beams have a width of 8 µm and a thickness of 10 µm. Gold pads for electrical connection were used in [19] and are retained in this design, however they are not used for this actuation technique. A scanning electron microscope (SEM) image of the fabricated device can be seen in Fig. 1.

B. Stress Analysis

To create an accurate FEA of the devices, their exhibited stresses after fabrication required characterization due to discrepancies between initially measured material properties and those described by Miller et al [27], who used the same fabrication process for their 10 µm thick single crystal silicon devices. The single crystal silicon layer of the VFM is subject to a through-thickness stress gradient due to polishing and doping processes during fabrication. This gradient, together with a compressive residual stress, leads to an initial concave curvature of the mirror surface prior to deposition of the gold layer. The stress gradient can be directly related to the curvature through analysis of the bending moment M. The bending moment due to a stress gradient can be evaluated using [28]:

$$M = \Delta\sigma I , \quad (1)$$

where $\Delta\sigma$ is the stress gradient and I is the moment of inertia. The bending moment is also directly related to the curvature κ using [29]:

$$\kappa = \frac{1}{ROC} = \frac{M}{EI} , \quad (2)$$

where ROC is the radius of curvature and E is the Young's modulus. Using (1) and (2), one can obtain an equation for the stress gradient $\Delta\sigma$ relative to the curvature of a deflected beam in the form of:

$$\Delta\sigma = E\kappa \quad (3)$$

TABLE I
Measured Stress Gradient for Cantilevers Fabricated using the SOIMUMPs Process

Sample No.	Beam Length (µm)	κ (m^{-1})	Δσ (MPa/µm)
1	700	13.4	2.26
2	800	13.1	2.21
3	600	14.7	2.48
4	700	14.4	2.43
5	800	13.7	2.32
6	600	15.4	2.60
7	700	14.8	2.50
8	800	13.7	2.32
9	600	15.1	2.55
10	700	14.4	2.43
11	800	13.4	2.26
12	600	14.6	2.47
	Average value	14.2	2.40

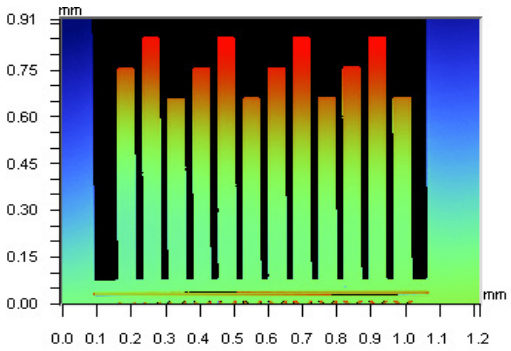

Fig. 2: VEECO optical profiler image showing the cantilever beams. Samples 1 to 12 from Table I range from left to right.

This article has been accepted for publication in a future issue of this journal, but has not been fully edited. Content may change prior to final publication. Citation information: DOI 10.1109/JSTQE.2014.2381464, IEEE Journal of Selected Topics in Quantum Electronics

TABLE II
MATERIAL PARAMETERS OF THE SIMULATED VFM

Parameter	Unit	Single crystal silicon	Gold
Young's modulus	GPa	E_x=E_y=169 E_z=130	57
Poisson ratio	-	ν_{yz}=0.36 ν_{zx}=0.28 ν_{xy}=0.064	0.44
Shear modulus	GPa	G_{yz}=G_{zx}=79.6 G_{xy}=50.9	-
Thermal expansion coefficient	ppm/K	2.53 at 290 K 2.62 at 300 K 2.84 at 330 K 3.24 at 400 K	13.7 at 200 K 14.2 at 293 K 15.4 at 500 K
Density	kg/m^3	2330	14300
Residual stress	MPa	-3.9	200.4
Stress gradient	MPa/μm	2.40	-

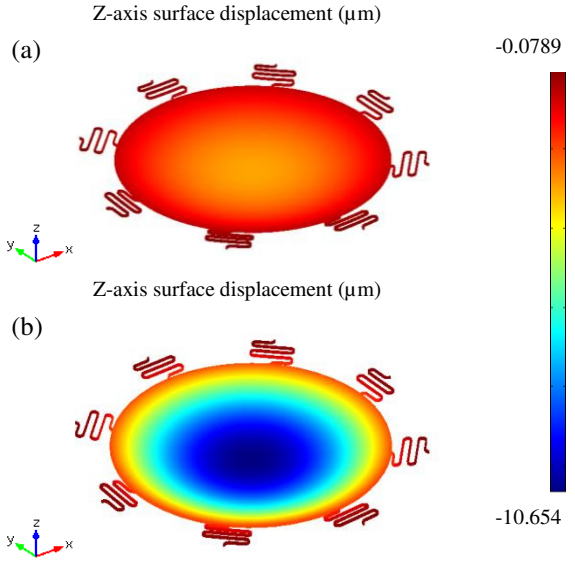

Fig. 3: Simulated surface displacement of (a) the single crystal silicon device layer only and (b) the VFM with gold-coated aperture at room temperature.

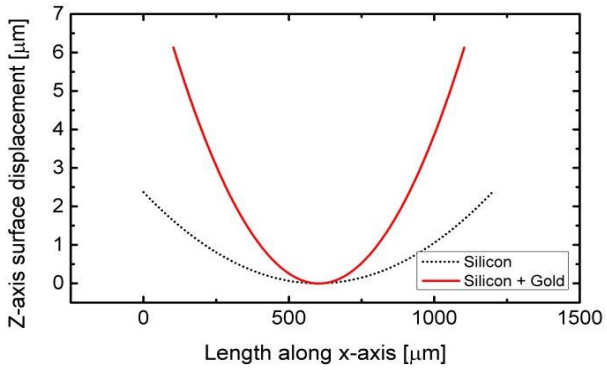

Fig. 4: Surface displacement of the simulated silicon layer only and the simulated VFM with silicon and gold, at room temperature, along the x-axis of the mirror surface.

To evaluate the stress gradient of our device, 10 μm thick, 50 μm wide cantilever beams of lengths 600 μm, 700 μm and 800 μm were fabricated using the same SOIMUMPs fabrication without the deposition of the gold layer. This cantilever test structure can be seen in Fig. 2. The ROCs of the test beams were measured using a VEECO NT1100 optical profiler, and hence the curvature was obtained by taking the reciprocal of these values. These values, together with calculated values for the stress gradient using (3), are shown in Table I. A value of 169 GPa was used for the Young's modulus of single crystal silicon [30], accounting for the anisotropy of single crystal silicon. The average value for the stress gradient of the cantilever beams was calculated to be 2.40 MPa/μm.

The deposition of the gold layer on the VFM resulted in an additional tensile residual stress, providing a measured ROC of 20 mm (κ=50 m^{-1}) at a temperature of 20 °C. The residual stress in the gold layer, σ_{au}, can be calculated using the Stoney equation modified to consider the anisotropy of the single crystal silicon layer and symmetrical radii of curvature of the major axes [31]:

$$\sigma_{au} = \frac{E_{si}(\kappa_{si,au} - \kappa_{si})t_{si}^{\,2}}{6t_{au}(1-\nu_{si})}, \quad (4)$$

where ν is the Poisson ratio and t is the thickness, with the notations 'si' and 'au' representing silicon and gold respectively. Assuming ν=0.28 [30], the residual stress in the gold layer was calculated to be 200.4 MPa.

C. Finite Element Modeling

FEA results are highly dependent on the material parameters used. For this reason, simulations of the cantilever test beams and the VFM were compared to experimental measurements. The simulations were performed using the FEA software COMSOL Multiphysics, with the material parameters shown in Table II. A value of 57 GPa was used for the Young's modulus of the gold layer, similar to that calculated from cantilever mechanical deflection measurement techniques for thin-film gold [32],[33].

The cantilever test beams were modeled considering only the single crystal silicon material and applying the through-thickness stress gradient in the x-direction. A fixed constraint on one end face was implemented. Separate simulations for cantilever lengths of 600 μm, 700 μm and 800 μm were performed, resulting in an initial curvature of 14.2 m^{-1} for each model. This matches the average curvature value in Table I. The stress gradient was then applied to the full single crystal silicon micromirror model, shown in Fig. 3(a), in the x- and y-directions. Fixed constraints were placed at the outer end faces of the serpentine suspension beams. This resulted in a curvature of 13.2 m^{-1}; slightly lower than the measured curvature of the cantilever test beams. Finally the application of the 0.65 μm thick gold layer was implemented, resulting in a mirror surface profile shown in Fig. 3(b) using the parameters from Table II. At a VFM temperature of 20 °C, the

This article has been accepted for publication in a future issue of this journal, but has not been fully edited. Content may change prior to final publication. Citation information: DOI 10.1109/JSTQE.2014.2381464, IEEE Journal of Selected Topics in Quantum Electronics

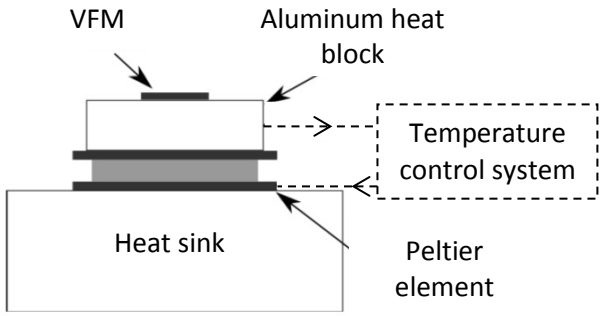

Fig. 5: Schematic of the VFM temperature control system.

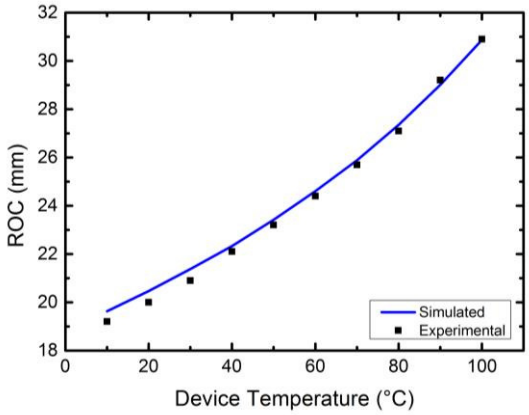

Fig. 6: Simulated and experimental ROC values for the VFM over a temperature range from 10 ^{0}C to 100 ^{0}C.

ROC was simulated to be 20.2 mm, similar to that measured experimentally. The simulated x-axis cross-section curvature profiles of the silicon micromirror and the VFM (silicon + gold) can be seen in Fig. 4.

III. Thermoelectric Actuation

Actuation of the VFM was performed using a thermoelectric device (Peltier element) integrated in a closed-loop temperature feedback system, as shown in Fig. 5. The MEMS chip, on which the VFM is fabricated, was secured on an aluminum block using thermal paste to enhance heat transfer to the device. Measurement of the temperature of the aluminum block, using a thermistor, allowed closed-loop control of the VFM temperature. The temperature of the VFM was varied from 10 °C to 100 °C in intermediate steps of 10 °C, allowing sufficient time at each step for the device to reach thermal equilibrium. The ROC of the device, measured using a VEECO NT1100 optical profiler, varied from 19.2 mm to 30.9 mm over the respective temperature range.

Using the parameters from Table II, actuation of the VFM was simulated using COMSOL Multiphysics by altering the temperature of the device. A parametric temperature sweep matching the experimental settings was performed. As observed in Fig. 6, a strong overlap between simulated and experimental ROC values is present. The simulated ROC values were measured on the [100], [010] and [110] axes and varied by less than 0.1 mm, indicating the anisotropy of the single crystal silicon layer had negligible effects on the simulated VFM performance.

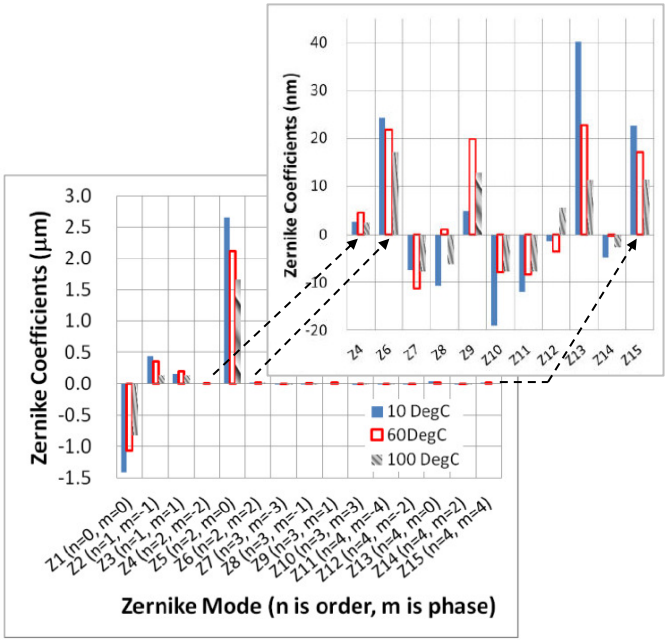

Fig. 7: Zernike coefficients of the VFM surface under experimental actuation at temperatures of 10 ^{0}C, 60 ^{0}C and 100 ^{0}C.

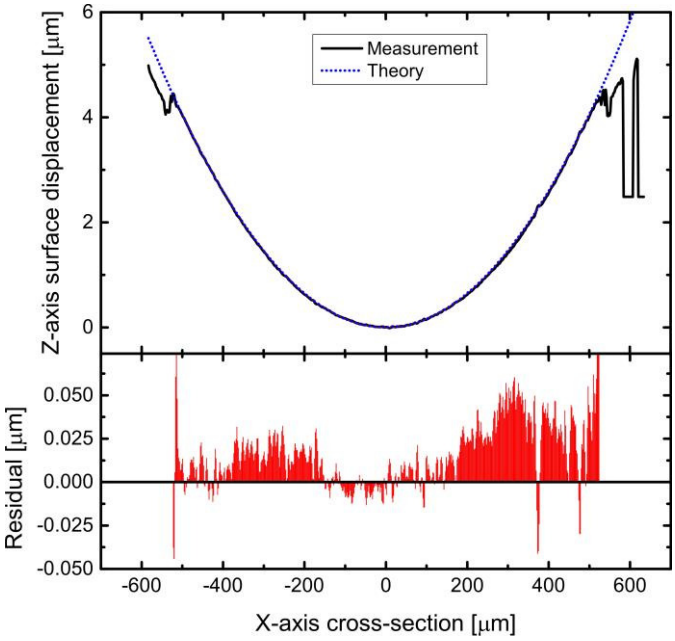

Fig. 8: The upper plot displays a comparison of the measured VFM surface profile at 100 °C to a theoretical parabola (deviations at each extreme represent the step between the coating and the micromirror and then the edge of the micromirror surface). The lower plot displays the residual between the theoretical and experimental curvature profiles.

The optical aberrations present in the VFM were quantified using Zernike polynomials [34], where a MATLAB program was used to calculate the Zernike coefficients from the measured surface profiles [35]. Fig. 7 shows the first 15 Zernike coefficients at VFM temperatures of 10 °C, 60 °C and 100 °C. The piston term, Z_1, and the tilt terms, Z_2 and Z_3, quantify the alignment of the measurement process and

This article has been accepted for publication in a future issue of this journal, but has not been fully edited. Content may change prior to final publication. Citation information: DOI 10.1109/JSTQE.2014.2381464, IEEE Journal of Selected Topics in Quantum Electronics

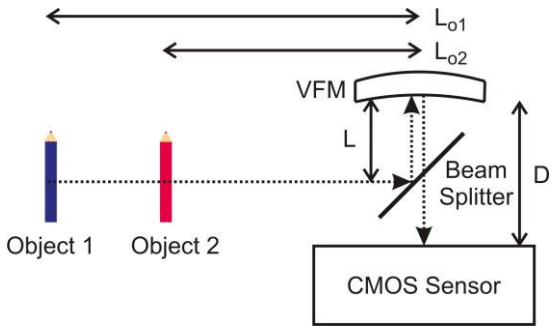

Fig. 9: Optical imaging system configuration, showing two objects located at total distances of $L+L_{o1}$ and $L+L_{o2}$ from the VFM. Reflected light from the objects is focused onto a CMOS sensor via a 50/50 beam splitter and the VFM, located at a distance D from the sensor.

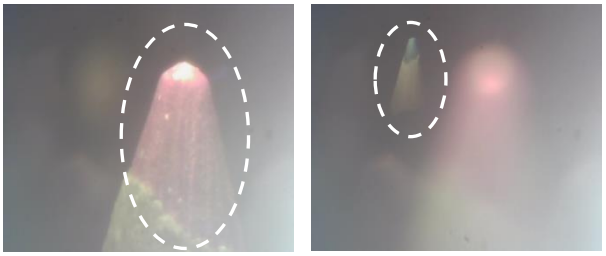

(a) $L_{o,min}$ = 23 mm (b) $L_{o,max}$ = 235 mm

Fig. 10: Images recorded by the CMOS sensor in the optical imaging system with objects placed at (a) $L_{o,min}$=23 mm and (b) $L_{o,max}$=235 mm from the sensor. The circled areas represent the position of the respective focal planes.

therefore do not contribute to the imaging performance of the VFM. The dominant coefficient is Z_5, the defocus term, with a value of 2.65 µm at 10 °C which decreases to 1.65 µm at 100 °C. The remaining modes demonstrate coefficients in the nm-range (e.g. astigmatism, coma, trefoil and spherical aberration) rendering them negligible, overall indicating a parabolic surface profile. This VFM actuation technique is therefore capable of producing near-aberration-free imaging across the entire actuation range. Fig. 8 shows a comparison of the measured surface profile of the VFM under actuation at 100 °C and a parabolic fit with equation $y=0.0001575x^2$, where x and y are both in µm. This was chosen to provide the best combined match to both simulated and measured profiles, with the residuals between the measured profile and the spherical fit being below 60 nm throughout the coated mirror surface profile.

IV. Implementation in an Optical Imaging System

To further assess the performance of the VFM it was implemented in an optical imaging system, shown in Fig. 9. Light from the objects was reflected towards the VFM using a 50/50 beam splitter, and then focused by the VFM onto a CMOS sensor located at a distance D from the VFM. The minimum and maximum object distances, $L_{o,min}$ and $L_{o,max}$, can be calculated using:

$$L_{o,min} = \frac{D \times ROC_{min}}{2D - ROC_{min}} \quad (5)$$

$$L_{o,max} = \frac{D \times ROC_{max}}{2D - ROC_{max}} \quad (6)$$

where ROC_{min} and ROC_{max} are the ROCs of the VFM at 10 °C and 100 °C respectively. When the CMOS sensor is located at a distance of 16.5 mm from the VFM, the calculated minimum and maximum distances are 23 mm and 235 mm respectively corresponding to a focal plane variation of 212 mm. This is a 57% increase over the results achieved in [19]. The imaging system was assessed by placing two objects, a red and a blue pencil, at the minimum and maximum object distances, corresponding to $L+L_{o2}$ and $L+L_{o1}$ respectively in Fig. 9. This resulted in sharp imaging of the objects as the VFM was actuated to both extremes, as shown in Fig. 10.

V. Discussion

The previous actuation principles for this VFM device were limited by current-induced heat in the suspension springs (which can lead to thermal damaging without current limitation) and the sensitivity to ambient temperature. Furthermore, laser illumination effects would be dependent on the size, shape and location of the beam on the VFM surface. The use of a Peltier element does not exhibit any of these limitations. The limiting factors of using this technique are the effectiveness of the heat conduction to the VFM and the operating range, stability and size of the Peltier device.

The size limitation of the actuator can be eliminated by the use of thin-film thermoelectric coatings, which have not yet been feasibly demonstrated for MEMS-scale imaging applications. A more compact device following the arrangement of Fig. 5 could also be implemented using a smaller Peltier element, meaning a smaller heat conduction plate and also reduced electrical power consumption. Relating to the micromirror itself, the size of the active region of the micromirror affects the imaging performance. In Fig. 7, the Zernike coefficients indicate aberrations at around λ/15 for visible light. However, the central region of the micromirror better matches the theoretical parabolic surface profile compared to the outer edges, as seen in Fig. 8. This is due to tension at the interface of the micromirror and the suspension springs. Hence, a smaller active region on the micromirror would improve the imaging quality of the device.

In terms of performance, the tracking range was demonstrated to increase by 57% using the Peltier element, compared to previous electrothermal and optothermal techniques. For the FEA models, accuracy is highly dependent on the device material properties used in the analysis. The uncertainty of Young's modulus is notorious for thin-film materials, meaning careful consideration of the material properties must be taken. If one would use the bulk Young's modulus of gold, 79 GPa, an increase of 20% in ROC

This article has been accepted for publication in a future issue of this journal, but has not been fully edited. Content may change prior to final publication. Citation information: DOI 10.1109/JSTQE.2014.2381464, IEEE Journal of Selected Topics in Quantum Electronics

variation over the actuation range would be observed compared to the thin-film gold parameters used in this work, conveying the sensitivity of the models to this parameter. A significant increase (>10%) in each respective ROC value would also be observed.

VI. Conclusion

A bimorph, varifocal micromirror actuated using a Peltier element was experimentally characterized and modeled by FEA. Actuation of the VFM over a temperature range from 10 ^{0}C to 100 ^{0}C resulted in a ROC range of 11.7 mm (19.2 mm to 30.9 mm). Simulated mirror surface curvatures are in excellent agreement with these results, yielding a strong match between FEA and experimental measurements. Zernike coefficients were evaluated for the VFM under multiple actuation conditions and illustrated that the main contribution to optical aberrations came from the defocus term, whilst negligible higher order aberrations were observed. This near-aberration-free imaging device was demonstrated in a compact optical imaging system, showing a focal plane variation of 212 mm (23 mm to 235 mm) with high quality images of two objects located at each extreme from the VFM. The observed performance enhancement using this actuation principle provides avenues for future work, for example reducing the size of the VFM actuation system to allow compatibility with compact imaging systems. An example of this would be the use of conformal, thin-film thermoelectric coatings, such as Sb_2Te_3 or Bi_2Te_3, deposited on the rear surface of the VFM which would allow direct alteration of device temperature, yielding an integrated actuation device. With a more widespread availability these could be used for actuation of VFMs in the future.

VII. References

[1] D. L. Dickensheets, "Requirements of MEMS membrane mirrors for focus adjustment and aberration correction in endoscopic confocal and optical coherence tomography imaging instruments," Journal of Micro/Nanolithography, MEMS and MOEMS, Vol. 7 (2), pp. 021008, Apr. 2008.

[2] S. J. Lukes, D. L. Dickensheets, "Agile scanning using a MEMS focus control mirror in a commercial confocal microscope," Three-Dimensional and Multidimensional Microscopy: Image Acquisition and Processing XXI, San Francisco, CA, 2014, pp. 89490W.

[3] J. M. Moghimi, K. N. Chattergoon, R. C. Wilson and D. L. Dickensheets, "High Speed Focus Control MEMS Mirror With Controlled Air Damping for Vital Microscopy," Journal of Microelectromechanical Systems, Vol. 22 (4), pp. 938-948, Aug. 2013.

[4] J. M. Jabbour, B. H. Malik, C. Olsovsky, R. Cuenca, S. Cheng, J. A. Jo, Y-S. L. Cheng, J. M. Wright and K. C. Maitland, "Optical axial scanning in confocal microscopy using an electrically tunable lens," Biomedical Optics Express, Vol. 5 (2), pp. 645-652, Feb. 2014.

[5] T. Sasaki and K. Hane, "A confocal laser scanning endoscope using a varifocal scanning mirror," Solid-State Sensors, Actuators and Microsystems, Transducers and Eurosensors XXVII, 17th International Conference on, Barcelona, 2013, pp. 1412-1415.

[6] B. Qi, P. A. Himmer, M. L. Gordon, V. X. D. Yang, D. L. Dickensheets and A. I. Vitkin, "Dynamic focus control in high-speed optical coherence tomography based on a microelectromechanical mirror," Optics Communications, Vol. 232 (1-6), pp. 123-128, Mar. 2004.

[7] L. Sherman, J. Y. Ye, O. Albert and T. B. Norris, "Adaptive correction of depth-induced aberrations in multiphoton scanning microscopy using a deformable mirror," Journal of Microscopy, Vol. 206 (1), pp. 65-71, Apr. 2002.

[8] H-T. Hsieh, H-C. Wei, M-H. Lin, W-Y. Hsu, Y-C. Cheng and G-D. J. Su, "Thin autofocus camera module by a large-stroke micromachined deformable mirror," Optics Express, Vol. 18 (11), pp. 11097-11104, July 2010.

[9] T. Sasaki, D. Sato and K. Hane, "Displacement-amplified dynamic varifocal mirror using mechanical resonance," Optical MEMS and Nanophotonics, 2013 International Conference on, Kanazawa, 2013, pp. 161-162.

[10] R. Hokari and K. Hane, "A Varifocal Convex Micromirror Driven by a Bending Moment," Journal of Selected Topics in Quantum Electronics, Vol. 15 (5), pp. 1310-1316, Sept.-Oct. 2009.

[11] M. Strathman, Y. Liu, X. Li and L. Y. Lin, "Dynamic focus-tracking MEMS scanning micromirror with low actuation voltages for endoscopic imaging," Optics Express, Vol. 21 (20), pp. 23934-41, Oct. 2013.

[12] S. J. Lukes and D. L. Dickensheets, "SU-8 2002 Surface Micromachined Deformable Membrane Mirrors," Journal of Microelectromechanical Systems, Vol. 22 (1), pp. 94-106, Feb. 2013.

[13] C. Knoernschild, C. Kim, B. Liu, F. P. Lu and J. Kim, "MEMS-based optical beam steering system for quantum information processing in two-dimensional atomic systems," Optics Letters, Vol. 33 (3), pp. 273-275, Feb. 2008.

[14] A. Ishii, S. Sugiyama, J-I. Sakai, S. Hirai and T. Ochi, "Constant magnification focusing using a varifocal mirror and its application to 3-D imaging," Proc. SPIE 4902, Optomechatronic Systems III, Stuttgart, 2002, pp. 238.

[15] M. J. Mescher, L. M. Vladimer and J. J. Bernstein, "A novel high-speed piezoelectric deformable varifocal mirror for optical applications," Micro Electro Mechanical Systems, 2002. The Fifteenth IEEE International Conference on, Las Vegas, NV, 2002, pp. 511-515.

[16] M. Stürmer, M. C. Wapler, J. Brunne and U. Wallrabe, "Focusing mirror with tunable eccentricity," Optical MEMS and Nanophotonics, 2013 International Conference on, Kanazawa, 2013, pp. 159-160.

[17] A. A. Alzaydi, J. T. W. Yeow and S. L. Lee, "Hydraulic controlled polyester-based micro adaptive mirror with adjustable focal length," Mechatronics, Vol. 18 (2), pp. 61-70, Mar. 2008.

[18] W. Liu and J. J. Talghader, "Current-controlled curvature of coated micromirrors," Optics Letters, Vol. 28 (11), pp. 932-934, June 2003.

[19] L. Li, R. Li, W. Lubeigt and D. Uttamchandani, "Design, Simulation, and Characterization of a Bimorph Varifocal Micromirror and Its Application in an Optical Imaging System," Journal of Microelectromechanical Systems, Vol. 22 (2), pp. 285-294, Apr. 2013.

[20] M. J. Moghimi, C. Wilson and D. L. Dickensheets, "Electrostatic-pneumatic membrane mirror with positive or negative variable optical power," Proc. SPIE 8617, MEMS Adaptive Optics VII, San Francisco, CA, 2013, pp. 861707.

[21] T. Sasaki and K. Hane, "Varifocal Micromirror Integrated With Comb-Drive Scanner on Silicon-on-Insulator Wafer," Journal of Microelectromechanical Systems, Vol. 21 (4), pp. 971-980, Aug. 2012.

[22] L. M. Gonçalves, P. Alpuim, A. G. Rolo and J. H. Correia, "Thermal co-evaporation of Sb_2Te_3 thin-films optimized for thermoelectric applications," Thin Solid Films, Vol. 519 (13), pp. 4152-4157, Apr. 2011.

[23] T. Sarnet, T. Hatanpää, E. Puukilainen, M. Mattinen, M. Vehkamäki, K. Mizohata, M. Ritala and M. Leskelä, "Atomic Layer Deposition and Characterization of Bi_2Te_3 Thin Films," Journal of Physical Chemistry A, DOI: 10.1021/jp5063429 [Online)] Available: http://pubs.acs.org/doi/abs/10.1021/jp5063429.

[24] T. Huesgen, P. Woias and N. Kockmann, "Design and fabrication of MEMS thermoelectric generators with high temperature efficiency," Sensor and Actuators A: Physical, Vol. 145-146, pp. 423-429, July-Aug. 2008.

[25] A. Boulouz, A. Giani, B. Sorli, L. Koutti, A. Massaq and F. Pascal-Delannoy, "Fabrication of Thermoelectric Sensor and Cooling Devices Based in Elaborated Bismuth-Telluride Alloy Thin Films," Journal of Materials, Vol. 2014 (1), 2014, [Online] Available: http://www.hindawi.com/journals/jma/2014/430410/.

[26] A. Cowen, G. Hames, D. Monk, S. Wilcenski and B. Hardy, SOIMUMPs Design Handbook, MEMSCAP Inc., Revision 8.0 Ed., [Online] Available: http://www.memscap.com.

[27] D. C. Miller, B. L. Boyce, M. T. Dugger, T. E. Buchheit and K. Gall, "Characteristics of a commercially available silicon-on-insulator MEMS material," Sensors and Actuators A: Physical, Vol. 138 (1), pp. 130-144, July 2007.

[28] G. M. Rebeiz, "Mechanical Modeling of MEMS Devices: Static Analysis" in RF MEMS: Theory, Design, and Technology, John Wiley and Sons, Inc., Hoboken, NJ, USA, 2004, pp. 34-36.

[29] J. Case, Lord A. Chilver and C. T. F. Ross, "Deflection of beams" in Strength of Materials and Structures, 4th Ed., Butterworth-Heinemann, Jordan Hill, Oxford, UK, 2003, pp. 295-300.

[30] M. A. Hopcroft, W. D. Nix and T. W. Kenny, "What is the Young's Modulus of Silicon?," Journal of Microelectromechanical Systems, Vol. 19 (2), pp. 229-238, Apr. 2010.

[31] D. C. Miller, C. F. Herrmann, H. J. Maier, S. M. George, C. R. Stoldt and K. Gall, "Thermo-mechanical evolution of multilayer thin films: Part I. Mechanical behavior of Au/Cr/Si microcantilevers," Thin Solid Films, Vol. 515 (6), pp. 3208-3223, Feb. 2007.

[32] T. P. Weihs, S. Hong, J. C. Bravman and W. D. Nix, "Mechanical deflection of cantilever microbeams: A new technique for testing the mechanical properties of thin films," Journal of Materials Research, Vol. 3 (5), pp. 931-942, May 1988.

[33] H. D. Espinosa and B. C. Prorok, "Size effects on the mechanical behavior of gold thin films," Journal of Materials Science, Vol. 38 (20), pp. 4125-4128, Oct. 2003.

[34] R. W. Gray and J. M. Howard, "A Matlab function to work with Zernike polynomials over circular and non-circular pupils," in Zernike Calc. Natick, MA: The Mathworks, Inc., Oct. 2011, [Online] Available: http://www.mathworks.com/matlabcentral/fileexchange/33330-zernikecalc.

[35] J. Schwiegerling, "Scaling Zernike expansion coefficients to different pupil sizes," Journal of the Optical Society of America A, Vol. 19 (10), pp. 1937-1945, Oct. 2002.

Alan Paterson was born near Glasgow, Scotland in 1990. He received the MEng degree in Electronic and Electrical Engineering from the University of Strathclyde, Glasgow, Scotland in 2013.

Currently he is undergoing a PhD project in the Centre for Microsystems and Photonics at the University of Strathclyde, involving the incorporation of MEMS into solid-state laser cavities as active tuning elements.

Ralf Bauer received the Dipl.-Ing. degree in Mechatronics from the University of Erlangen-Nuernberg, Germany in 2010, and the Ph.D. degree from the University of Strathclyde, Glasgow, U.K., in 2013 for work on MEMS micromirrors as active intracavity devices in solid-state lasers.

He is currently a Post-doctoral Research Associate in the Centre for Microsystems and Photonics, University of Strathclyde, working on the integration of MEMS devices in miniature photoacoustic spectroscopy gas sensors and optical sensors for trace gas detection. His research interests include the development and integration of MEMS in optical systems and laser systems.

Dr. Bauer is a member of the Optical Society and former vice-president and current member of the University of Strathclyde student chapter of the OSA, IOP and EPS.

Li Li received the joint B.Eng. degree in electronic and electrical engineering from North China Electric Power University, Beijing, China, and the University of Strathclyde, Glasgow, U.K., in 2008, and the M.Sc. degree in control, communication, and digital signal processing from the University of Strathclyde, Glasgow, U.K., in 2009. She was awarded her Ph.D. in 2013 in the Centre for Microsystems and Photonics, Department of Electronic and Electrical Engineering, University of Strathclyde.

Her main research interests are the design, characterization, and finite element method simulation of MEMS devices.

Walter Lubeigt received the Engineering Diploma degree in opto-electronic systems from the Ecole Supérieure des Procédés Electroniques et Optiques, University of Orléans, France in 2001. He then received the PhD. degree from the University of Strathclyde, Glasgow, U.K. in 2006 for work on solid-state laser performance enhancement using intracavity adaptive optics techniques.

He subsequently worked on the development of diamond Raman lasers at the Institute of Photonics, University of Strathclyde. In 2010, he joined the Centre for Microsystems and Photonics, University of Strathclyde, as a John Anderson Research Lecturer. His current research interests include the development of MEMS-controlled solid-state lasers, the use of intracavity adaptive optics to improve the performance of solid-state Raman lasers and the development of novel laser systems for environmental remote sensing.

Deepak Uttamchandani (SM'05) received the Ph.D. degree from University College London, London, U.K., in the area of optical fiber sensors, in 1985.

He is currently the Head of the Centre for Microsystems and Photonics, University of Strathclyde, Glasgow, U.K. His early research in MEMS concentrated on optothermal microresonator sensors and in investigating techniques for general MEMS material characterization using MEMS micromechanical resonators. His recent research has concentrated on system applications of optical MEMS including intracavity MEMS-based laser systems, MEMS-based directional microphones and MEMS-based single-pixel imaging systems. He has also published in the field of optical sensors including subwavelength tip-based Raman spectroscopy, which has contributed to the development of tip-enhanced Raman spectroscopy and in the area of in situ intraocular drug detection systems via optical spectroscopy in the living eye.